JOURNAL OF SPACECRAFT AND ROCKETS
Vol. 43, No. 1, January–February 2006

Finite Volume Numerical Methods for Aeroheating Rate Calculations from Infrared Thermographic Data

Kamran Daryabeigi,[*] Scott A. Berry,[†] Thomas J. Horvath,[†] and Robert J. Nowak[‡]
NASA Langley Research Center, Hampton, Virginia 23681

The use of multidimensional finite volume heat-conduction techniques for calculating aeroheating rates from measured global surface temperatures on hypersonic wind-tunnel models was investigated. Both direct and inverse finite volume techniques were investigated and compared with the standard one-dimensional semi-infinite technique. Global transient surface temperatures were measured using an infrared thermographic technique on a 0.333-scale model of the Hyper-X forebody in the NASA Langley Research Center 20-Inch Mach 6 Air tunnel. In these tests the effectiveness of vortices generated via gas injection for initiating hypersonic transition on the Hyper-X forebody was investigated. An array of streamwise-orientated heating striations was generated and visualized downstream of the gas injection sites. In regions without significant spatial temperature gradients, one-dimensional techniques provided accurate aeroheating rates. In regions with sharp temperature gradients caused by striation patterns, multidimensional heat-transfer techniques were necessary to obtain more accurate heating rates. The use of the one-dimensional technique resulted in differences of ±20% in the calculated heating rates compared to two-dimensional analysis because it did not account for lateral heat conduction in the model.

Nomenclature

c = specific heat, $\mathrm{J \cdot kg^{-1} \cdot K^{-1}}$
Fo = Fourier number
H = enthalpy, $\mathrm{J \cdot kg^{-1}}$
h = enthalpy-based heat-transfer coefficient, $\mathrm{kg \cdot m^{-2} \cdot s^{-1}}$
h_{ref} = reference heat-transfer coefficient, $\mathrm{kg \cdot m^{-2} \cdot s^{-1}}$
k = thermal conductivity, $\mathrm{W \cdot m^{-1} \cdot K^{-1}}$
L = length, m
L_x = length of first Macor insert, m
L_y = width of first Macor insert, m
L_z = thickness of Macor inserts, m
M = Mach number
$\hat{\boldsymbol{n}}$ = unit normal vector
q'' = heat flux, $\mathrm{W \cdot m^{-2}}$
Re = Reynolds number
S = sum of square of errors
T = temperature, K
T_0 = initial (prerun) temperature, K
t = run time (measured from initiation of model injection), s
t_{corr} = correction time, s
t_{eff} = effective time, s
t_1 = time model is at test section centerline, s
x = local coordinate along model length
y = local coordinate along model width
z = local coordinate along model thickness
α = thermal diffusivity, $\mathrm{m^2 \cdot s^{-1}}$
β = thermal product, $\sqrt{(\rho c k)}$, $\mathrm{J \cdot m^{-2} \cdot K^{-1} \cdot s^{-0.5}}$
ε = emittance
ρ = density, $\mathrm{kg \cdot m^{-3}}$
σ = Stefan–Boltzmann constant, 5.67×10^{-8} $\mathrm{W \cdot m^{-2} \cdot K^{-4}}$

Subscripts

aw = adiabatic-wall condition
m = measured
p = predicted
tw = tunnel wall
$t1$ = reservoir conditions
$t2$ = stagnation conditions behind normal shock
w = wall condition
0 = initial
∞ = freestream static condition

Introduction

ONE of the standard techniques for calculating aeroheating rates from measured transient surface temperatures on hypersonic wind-tunnel models is the one-dimensional semi-infinite solid conduction method. This method was originally developed for use with discrete temperature sensors, such as thin-film resistance gauges.[1] The semi-infinite technique assumes that heat does not noticeably diffuse to the back surface of the model, so that the back surface temperature does not vary with time. It is also assumed that there is no lateral heat conduction so that heat is conducted only in the direction of the model thickness from the top surface (surface exposed to aeroheating) to the back surface. This assumption is necessary when using discrete temperature sensors, because, as a result of limitations on the number and spacing of the sensors that can be installed on the model, multidimensional conduction cannot be considered. There are several limitations to the use of the one-dimensional semi-infinite method. The semi-infinite assumption is only valid for a specific time duration that is a function of model thickness and thermophysical properties. The method assumes constant thermophysical properties. Furthermore, this technique is not suitable for regions with sharp temperature gradients across the surface, because lateral heat conduction can be significant compared to through-the-thickness heat conduction.

To overcome limitations on the number of discrete sensors that can be installed on models, optical techniques such as infrared and phosphor thermal imaging have been used for providing global aeroheating data on hypersonic wind-tunnel models. The phosphor thermography technique is routinely used for hypersonic wind-tunnel aeroheating measurements.[2] The accuracy of infrared thermal imaging for transient surface-temperature measurements on a flat plate model in subsonic flow has been evaluated by comparison with surface-mounted thermocouples.[3] This technique has been used for

---

Presented as Paper 2003-3634 at the 36th Thermophysics Conference, Orlando, FL, 23–26 June 2003; received 9 November 2004; revision received 18 May 2005; accepted for publication 24 May 2005. This material is declared a work of the U.S. Government and is not subject to copyright protection in the United States. Copies of this paper may be made for personal or internal use, on condition that the copier pay the $10.00 per-copy fee to the Copyright Clearance Center, Inc., 222 Rosewood Drive, Danvers, MA 01923; include the code 0022-4650/06 $10.00 in correspondence with the CCC.

[*] Aerospace Technologist, MS 396, Metal and Thermal Structures Branch. Senior Member AIAA.

[†] Aerospace Technologist, MS 408A, Aerothermodynamics Branch. Member AIAA.

[‡] Research Scientist, MS 408A, Aerothermodynamics Branch. Member AIAA.

aeroheating calculations on hypersonic wind-tunnel models[4,5] and for in-flight surface-temperature measurements on the space Shuttle Orbiter.[6,7] The one-dimensional semi-infinite technique is the standard method used with thermal imaging techniques, even though the availability of whole-field surface-temperature distributions lends itself to using numerical multidimensional thermal analysis. The one-dimensional semi-infinite method yields a simple analytical solution,[8] whereas multidimensional solid conduction analysis requires numerical thermal analysis software and complete modeling of the geometry of the wind-tunnel model.

Numerical techniques have previously been used with discrete sensors to overcome some of the one-dimensional semi-infinite limitations. The one-dimensional finite volume technique has been used for calculating aeroheating rates from discrete sensors on hypersonic wind-tunnel models.[9,10] An inverse two-dimensional finite element numerical technique has been used in conjunction with temperature measurements from a linear array of closely spaced thin film gauges to obtain heating rate distributions in the region of shock impingement on a cylinder in Mach 6 flow.[11] This technique resulted in higher peak heating rate predictions at shock impingement locations compared to the one-dimensional semi-infinite technique. Transient axisymmetric finite element thermal analysis has been used in conjunction with coaxial thermocouple data for hypersonic wind-tunnel tests on a double-cone experiment.[12]

To investigate multidimensional finite volume heat-conduction techniques with global thermal imaging data, a series of runs was conducted as a subset of an overall experimental program for evaluating gas injection for tripping the boundary layer on a 0.333-scale Hyper-X forebody model. This tripping mechanism produced an array of streamwise orientated heating striations downstream of the gas injection sites. Various solid-trip configurations were previously investigated on this 0.333-scale Hyper-X forebody model.[13] The overall test program was a comprehensive study to investigate the effectiveness of gas injection for hypersonic boundary-layer transition and included more than 80 wind-tunnel runs. It used phosphor thermography for aeroheating measurements and included oil-flow-visualization runs. The runs reported here were a small subset of the overall test program and concentrated on evaluation of multidimentional solid conduction numerical methods in conjunction with infrared thermographic techniques to study the striation heating downstream of the gas injection sites.

The main objective of this investigation was to compare one-dimensional and multidimensional finite volume methods with one-dimensional semi-infinite technique for predicting heating rates from global thermographic techniques in conventional blowdown hypersonic wind tunnels.

Experimental Methodology

Test Facility and Test Conditions

Aeroheating data were obtained on a 0.333-scale Hyper-X forebody model in the 20-Inch Mach 6 Air Tunnel of the NASA Langley Research Center Aerothermodynamics Laboratory.[14] This tunnel is a conventional blowdown tunnel with a 0.521 × 0.508 m (20.5 × 20 in.) test section. A detailed description of the facility and its associated instrumentation is found in Ref. 14. A bottom-mounted model injection system inserts models from a sheltered position to the tunnel centerline in approximately 1–2 s, and the typical duration of aeroheating tests in this facility is 5–10 s.

The nominal reservoir stagnation pressure and temperature for the two runs reported in the present study are presented in Table. 1. The reported flow conditions were based on the measured reservoir stagnation pressures and temperatures and recent unpublished tunnel calibrations. Both runs were conducted with the model at an angle of attack of 2 deg. Run 70 was a baseline test without gas injection into the boundary layer, whereas run 71 consisted of gas injection into the boundary layer. The total pressure of the gas injected into the boundary layer was measured in a manifold directly below the orifices and was 31.2 kPa. The total pressure was used to control the penetration depth of the jets compared to the boundary-layer thickness.

Table 1 Nominal tunnel flow conditions

Run number	$Re_\infty \times 10^6/\mathrm{m}$	M_∞	P_{t1}, MPa	T_{t1}, K	H_{t1}, KJ/kg	P_{t2}, MPa
70	7.34	5.94	0.864	503.4	506.9	0.027
71	7.36	5.94	0.865	503.9	506.4	0.027

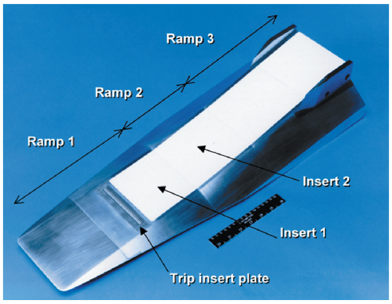

Fig. 1 Photograph of 0.333-scale Hyper-X forebody model with Macor inserts.

Model

A photograph of the 0.333-scale Hyper-X forebody model is shown in Fig. 1. This model is described in detail in Ref. 13 and was previously used for comparing the effectiveness of various hypersonic boundary-layer trip devices. The windward forebody model consisted of three flat ramps that provided a series of discrete non-isentropic flow compression surfaces simulating the engine external inlet ramps. The model was tested at a 2-deg angle of attack, and the first, second, and third ramps provided additional compressions of 2.5, 5.5, and 3 deg, respectively.

The 71.12-cm-long forebody model was built from aluminum and had a detachable stainless-steel leading edge (nose radius of 0.254 mm) and interchangeable measurement surface inserts. The length of the leading edge was 12.7 cm, whereas the trip station was 18.84 cm from the model leading edge. The trip insert plates consisted of several stainless-steel inserts with various orifice shapes and spacing for gas injection into the flow to trip the boundary layer. The specific trip insert plate used in this study consisted of a single row of 17 orifices, 0.25 mm in diameter with a 3.18-mm spacing. The remaining flat ramp sections were designed to accommodate either a Macor (a machinable glass ceramic, which is a registered trademark of Corning, Inc.) or aluminum set of inserts. The Macor and aluminum inserts were used for heat-transfer and flow-visualization studies, respectively. The Macor inserts were 6.35-mm thick. The leading edge of the first insert plate, 10.87 cm long and 12.9 cm wide, was 20.74 cm downstream of the model leading edge. The aeroheating data from the first Macor insert were used in this study. Because phosphor thermography was the main measurement system used for obtaining heating rates for the overall experimental program, the Macor substrates were coated with a 0.025-mm-thick mixture of phosphors suspended in a silica-based colloidal binder. A photograph of part of the model showing the leading edge, the trip insert plate with 17 orifices for gas injection, and the first Macor insert is shown in Fig. 2.

Test Technique

Model surface temperatures were measured using an infrared imaging system with an uncooled microbolometer-based focal plane array detector with 320 × 240 detector elements. The imager has a field of view of 24 × 18 deg and is sensitive to infrared radiation emitted in the 7–12-μm spectral range of the electromagnetic spectrum. An 8-in.-diam zinc-selenide window with antireflection coating to provide transmittance of 0.98 in the 7–14-μm spectral range was used for optical access to the test section. The imager produces 30 frames of images per second, and the data-acquisition hardware used provided real-time digital storage of five frames per second. The room-temperature, total (wavelength averaged), near-normal emittance of the Macor inserts with the applied surface phosphor coating was determined to be 0.88 using a heated cavity

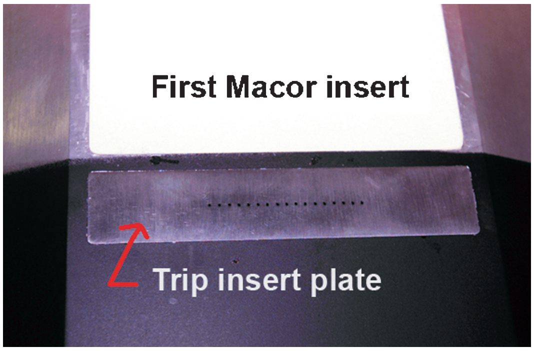

Fig. 2 Photograph of trip insert plate with 17 orifices and first Macor insert on the Hyper-X forebody model.

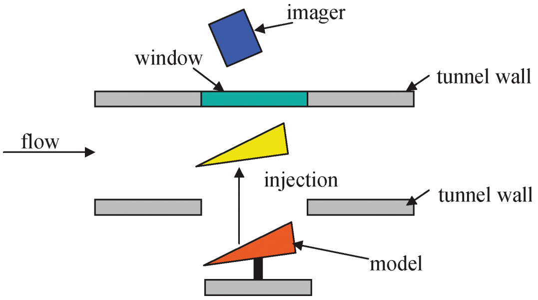

Fig. 3 Schematic of experimental setup.

reflectometer.[15] Joints between the Macor inserts corresponding to the location of ramp angle changes (Fig. 1) were used to geometrically locate the model in image mappings. Surface temperatures were measured on parts of the model leading edge, the entire first Macor insert, and part of the second Macor insert, but only the data from the first Macor insert were used in this study to compare various aeroheating calculation techniques. Model surface streamlines were obtained using the oil flow technique to correlate with aeroheating results. For oil flow tests, metal inserts used on the model were spray painted with black paint to enhance contrast with the white-pigmented oil, and surface streamlines were recorded using a conventional video camera.[13]

Test Procedure

To compare results from the multidimensional finite volume heat-conduction technique with the standard semi-infinite technique, a "prerun" image was obtained, which is the standard procedure used for data reduction using the semi-infinite technique with global optical techniques in conventional blowdown hypersonic wind tunnels with model injection systems.[2] This procedure consisted of injecting the model into the test section just before establishing tunnel flow and obtaining a prerun image of initial surface-temperature distribution across the model. Then the model was retracted. The tunnel underwent a "preheat" cycle, where the gas in the stagnation chamber was heated to the desired total temperature. After the flow was established, the model was injected into the test section, and the start of the injection process triggered the infrared imaging digital recording process at 0.2-s intervals. Figure 3 shows a schematic of the test setup. As the actual size of the target (first Macor insert) image varied during the model injection process, a mapping process was used with linear interpolation of data to map images obtained during injection process to the final image size (constant image size after model had reached the stationary position in the test section).

Solution Techniques

One-Dimensional Semi-Infinite Method

The one-dimensional semi-infinite solid conduction formulation with specified surface temperature boundary condition, typically used with discrete sensors, is not used with global thermographic techniques in conventional blowdown hypersonic wind tunnels with model injection systems because of various complications. First, continuous digital recording of whole images at 30 Hz requires significant image-processing hardware speed and storage space. Furthermore, mapping of temperature fields is required during the injection process because image size of the target varies until the model reaches its stationary position at the test-section centerline. Finally, surface-temperature data might not be available during the injection process for optical techniques requiring active illumination of target with ultraviolet excitation. The one-dimensional semi-infinite data-reduction method with convective boundary condition is typically used in these facilites and is used in this study as a basis of comparison with numerical methods. The governing equation is the constant property one-dimensional heat conduction equation, with an enthalpy-based convective boundary condition

$$-k\frac{\partial T}{\partial z}(0,t) = h[H_{\mathrm{aw}} - H_w(t)] \tag{1}$$

H_{aw} is the adiabatic wall enthalpy assumed to be equal to the total enthalpy (H_{t1} in Table. 1), and H_w is the wall enthalpy evaluated at wall temperature [$T_w = T(0,t)$]. The analytical solution is

$$T(z,t) = T_0 + \{H_{\mathrm{aw}}[T(0,t)/H_w(t)] - T_0\}$$
$$\times\left[\mathrm{erfc}(\eta) - \exp[hH_w z/T(0,t)k + \lambda^2]\,\mathrm{erfc}(\lambda+\eta)\right] \tag{2}$$

where T_0 is the initial temperature, typically obtained from the prerun image, and

$$\eta = z\big/2\sqrt{\alpha t} \tag{3a}$$

$$\lambda = hH_w(t)\sqrt{t}\big/T(0,t)\beta \tag{3b}$$

$$\beta = \sqrt{\rho c k} \tag{3c}$$

where erfc is the complimentary error function. At the surface ($z = 0$), the solution reduces to

$$\frac{T(0,t) - T_0}{[H_{\mathrm{aw}}/H_w(t)]T(0,t) - T_0} = 1 - e^{\lambda^2}\mathrm{erfc}\,\lambda \tag{4}$$

The measured surface temperature is used in Eq. (4) to solve for λ, which then yields the heat-transfer coefficient h from Eq. (3b). Because the formulation is for constant thermophysical properties, calculations are made using temperature-averaged properties.[2] The preceding calculations are performed for every point (pixel) in the image, assuming that heat transfer is only in the direction of model thickness. All that is needed to compute heat-transfer coefficient distributions over the model is the initial surface-temperature distribution, T_0 (typically from prerun) and temperature distribution at one instant of time after the model has reached the test-section centerline $T(0,t)$. This technique assumes that the heat-transfer coefficient distribution is time invariant. This assumption is not valid when the model is traversing through the test-section's boundary layer. To overcome this difficulty, the injection process is modeled as a delayed step heating, with the delay in the step corresponding to the time when the model has traversed halfway through the tunnel boundary layer.[2] The time it takes from the initiation of the injection process until the model traverses halfway through the tunnel boundary-layer edge is referred to as the correction time t_{corr} and is subtracted from the run time to obtain an effective time to be used in the preceding equations[2]:

$$t_{\mathrm{eff}} = t - t_{\mathrm{corr}} \tag{5}$$

where t is the actual run time, which is triggered when the injection system first starts to move. Then t_{eff} is used instead of t in Eqs. (2–4). This technique has been validated by aeroheating calculations on a 50.8-mm-diam hemisphere in Mach 10 flow[2] and has been applied to typical blunt-body configurations such as X-34[2] and X-33 (Ref. 16).

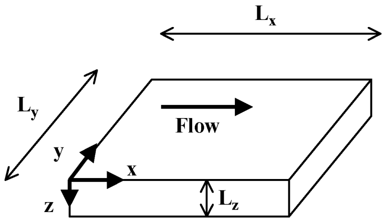

Fig. 4 Coordinate system and geometrical definitions for the first Macor insert.

Finite Volume Numerical Technique

As mentioned earlier, only the data from the first Macor insert are discussed in this study to simplify geometrical considerations and concentrate on the basic aeroheating calculation issues. Referring to Fig. 4 for local coordinate system and geometrical definitions, the governing three-dimensional diffusion equation and initial and boundary conditions used for the Macor insert were

$$\rho c \frac{\partial T}{\partial t} = \frac{\partial}{\partial x}\left(k\frac{\partial T}{\partial x}\right) + \frac{\partial}{\partial y}\left(k\frac{\partial T}{\partial y}\right) + \frac{\partial}{\partial z}\left(k\frac{\partial T}{\partial z}\right) \tag{6a}$$

$$T(x, y, z, 0) = \mathrm{g}(x, y, z) \tag{6b}$$

$$T(x, y, 0, t) = f(x, y, t) \tag{6c}$$

whereas, on all other boundaries,

$$\nabla T \cdot \hat{\boldsymbol{n}} = 0 \tag{6d}$$

For simplicity, it was assumed that adiabatic boundary conditions existed at the edges of the Macor insert ($y = 0$, $y = L_y$, $x = 0$, and $x = L_x$) [Eq. (6d)]. It was assumed that the model backface ($z = L_z$) is adiabatic [Eq. (6d)] and the top surface has a specified transient temperature distribution $f(x, y, t)$, measured using the optical thermographic technique [Eq. (6c)]. The backface adiabatic assumption is certainly valid during the time the semi-infinite assumption is valid. Furthermore, after the backface temperature begins to rise, the heat losses from the backface are typically low enough that the assumption of an adiabatic condition might not introduce large errors. For the direct finite volume technique, the initial temperature distribution for Eq. (6b) was obtained from the image at the beginning of injection process ($t = 0$ s), assuming uniform initial temperature distribution through the thickness at each pixel location.

The governing equations for the two- and one-dimensional finite volume techniques are subsets of the set of equations provided in Eqs. (6a–6d). For the one-dimensional case the dependence on x and y coordinates and the corresponding boundary conditions in these directions are eliminated. For the two-dimensional case the dependence on either the x or y coordinate and the corresponding boundary conditions in these directions are eliminated. The solution to this set of equations constitutes the direct solution method. In the present study, the equations were solved using a finite volume numerical method with variable thermophysical properties. The transient problem was solved using unconditionally stable implicit time-marching techniques[17]: Crank–Nicholson method for the one-dimensional case and alternating-direction-implicit method for the two- and three-dimensional cases. The governing equations and the derivative boundary conditions were formulated such that second-order accuracy could be achieved with truncation errors on the order of Δt^2 and $\Delta \boldsymbol{x}^2$, where Δt and $\Delta \boldsymbol{x}$ are the time step and spatial nodal spacing, respectively. For the results reported here 21 nodes were used in the z direction and 128 by 159 nodes in the y and x directions, respectively. The latter was dictated by the number of infrared image pixels across the top surface of the first Macor insert. Solutions obtained using 51 and 21 nodes in the z direction were similar, thus verifying that the through-thickness nodal spacing used was sufficient. The time step used was dictated by the digital storage interval of infrared images (0.2 s). Upon numerical solution of the governing equations, the convective heat-transfer coefficient h for the one-dimensional finite volume technique was calculated at each instant of time from conservation of energy for the surface volume elements:

$$-k(\Delta T/\Delta z)(x, y, 0, t) + \rho c \Delta z(\Delta T/\Delta t) + \varepsilon\sigma\left[T^4(x, y, 0, t) - T_{\mathrm{tw}}^4\right] = h(x, y, t)[H_{\mathrm{aw}} - H_w(x, y, t)] \tag{6e}$$

Δz is the thickness of the control volume around the node at the surface. This energy balance states that the convective heating is balanced by heat conduction into model, heat storage in the surface volume element, and heat radiated to the surroundings. For the three-dimensional finite volume technique solid conduction terms along the x and y directions were added to the energy balance in Eq. (6e).

In the inverse method, it is assumed that the surface is exposed to a time invariant but spatially variant heat-transfer coefficient. Therefore, Eq. (6e) is used as the boundary condition at the surface $z = 0$, whereas adiabatic boundary conditions are assumed for all of the other boundaries. Because the heat-transfer coefficients in Eq. (6e) are unknown, the conjugate gradient method for nonlinear parameter estimation[18] was used to estimate their values. This technique is an iterative numerical scheme, where a distribution of heat-transfer coefficients $h(x, y)$ is assumed; the numerical solution to the equation using this boundary condition is marched in time, and surface-temperature distributions are calculated. The comparison of measured and predicted transient surface temperatures over the test interval and the Jacobian matrix representing the derivatives of surface temperatures with respect to the heat-transfer coefficients is used to develop better estimates of $h(x, y)$. This iterative procedure is based on the minimization of the ordinary least-squares norm given by

$$S = \sum \left[T_m(x, y, 0, t) - T_p(x, y, 0, t)\right]^2 \tag{7}$$

where T_m and T_p are measured and predicted surface temperatures, respectively. The one-dimensional inverse method required estimating one heat-transfer coefficient at each measurement point on the image in an uncoupled manner. The two- and three-dimensional inverse methods required simultaneous estimation of either a vector of heat-transfer coefficient along a specific axis or an array of heat-transfer coefficients over the entire image, respectively. The computational effort increases tremendously as analysis is extended from two to three-dimensional. In their three-dimensional inverse method for calculating aeroheating rates form thermography data, Smith and Scott[19] found it necessary to divide the geometry into several patches, which were solved separately and then combined to obtain the full solution. As discussed in the subsequent presentation of results, it was found that two-dimensional inverse technique was sufficient for the present study.

For the inverse finite volume method, the governing conservation of energy equation (6a) was solved for time $t \geq t_1$, with t_1 corresponding to time when the model had reached the test-section centerline. The initial temperature distribution at time t_1 was

$$T(x, y, x, t_1) = g_1(x, y, z) \tag{8}$$

This initial temperature distribution was not known for $z > 0$, and the z variation was approximated at each pixel location by the analytical solution of one-dimensional semi-infinite conduction model, Eq. (2), at time t_1. The temperature distribution from the image obtained at $t = 0$ s was used instead of prerun data for T_0 in this equation. Any errors in the initial temperature distribution given in Eq. (8) will be corrected after a few time steps of the numerical solution because of the diffusive nature of heat conduction.

Uncertainty Analysis

A detailed uncertainty analysis[20] was performed to obtain uncertainty estimates for the calculated heat-transfer coefficients. The total uncertainty is the sum of the bias error and the precision error. It was assumed that the sources of bias uncertainty were the bias error in temperature measurement and the uncertainty in the thermophysical properties of the model material. The only source of precision error was assumed to be the random error in temperature measurement. The uncertainty in the thermal diffusivity and thermal conductivity data of Macor was ±7.3% (Ref. 21). A series of in situ calibrations was conducted at the wind tunnel by installing a blackbody radiation source in the center of the tunnel test section and measuring its temperature using the infrared imaging system through the same optical path used during actual wind-tunnel testing. The bias error (difference between temperature measurements using infrared imaging and the actual blackbody radiation source) was ±4 K for the temperature range of 300–420 K. The precision error for temperature measurement was calculated from the random noise associated with transient temperature measurements of the blackbody radiation source and was determined to be 1.06 K for a 95% confidence interval. The overall uncertainty for the heat-transfer coefficients reported in the present study was estimated[20] to be ±5.4%.

Results and Discussion

Results for the baseline run without gas injection (run 70) are presented to compare various techniques for calculating aeroheating rates. Then the results for the run with gas injection (run 71) are presented. Macor thermophysical properties were obtained from published results in Ref. 9. The convective heat-transfer rates were nondimensionalized with respect to a reference heat-transfer coefficient h_{ref} corresponding to the Fay and Riddell[22] stagnation-point heating on a 101.6-mm radius sphere. Only the surface temperature and aeroheating results on the first Macor insert are presented.

Run Without Gas Injection

The run without gas injection provided uniform surface temperature and aeroheating distributions across most of the surface area of the first Macor insert and was therefore used to compare one-dimensional and multidimensional direct and inverse finite volume methods with the semi-infinite technique. The longitudinal distribution of surface-temperature distribution along the centerline of the forebody model $(y/L_y = 0.5)$ at various times is shown in Fig. 5. Run time of 0 s corresponds to when the model injection was initiated. The model reached test-section centerline at 1.37 s, and the run lasted 8 s. The prerun data were arbitrarily set at -1 s. The lower temperatures at $x/L_x \geq 0.9$, evident at later times, were due to flow separation near the end of the first Macor insert caused by the adverse pressure gradient provided by the second ramp. The surface temperatures rose approximately 4 K from 0 to 8 s. The prerun temperatures were on the average 1.7 K cooler than at initiation of injection (0 s). The standard practice in using semi-infinite solution with convective boundary condition in conventional blowdown hypersonic wind tunnels with model injection systems is to assume that the prerun data provide the initial temperature distribution on the model. It is evident that the model in its retracted position during the preheat cycle experiences some heating and its temperature rises. For testing on blunt bodies at high Reynolds numbers when the model temperature can rise significantly during the test, this initial discrepancy in temperatures might not result in large errors.

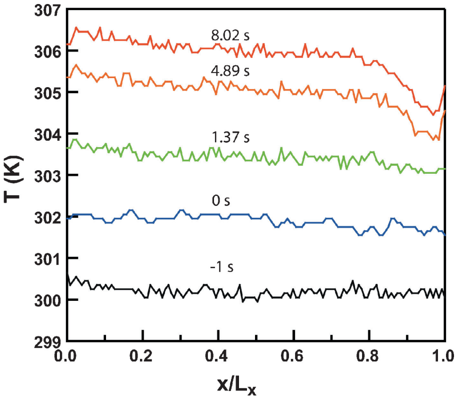

Fig. 5 Longitudinal variation of surface temperature at $y/L_y = 0.5$ at various times.

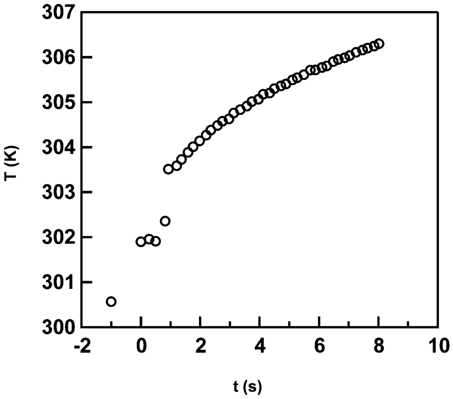

Fig. 6 Temporal variation of spanwise-averaged surface temperatures at $x/L_x = 0.25$.

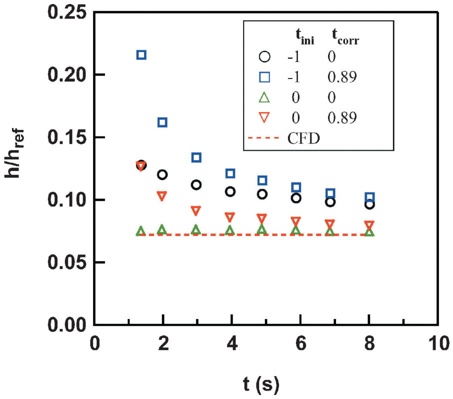

Fig. 7 Temporal variation of spanwise-averaged heating rates at $x/L_x = 0.25$ using semi-infinite technique.

To compare various techniques for prediction of heating rates, first average temperatures and heating rates (averaged spanwise over $0 \leq y/L_y \leq 1$) at $x/L_x = 0.25$ were investigated. The surface temperatures in the vicinity of this location were spatially uniform in the longitudinal direction, thus enabling comparison of various one-dimensional methods. The variation of spanwise-averaged temperature at this longitudinal position with time is presented in Fig. 6. The model reached test-section centerline at 1.37 s. The prerun data are 1.3 K cooler than at initiation of injection (0 s). The temperature then stayed almost constant during the first 0.5 s of injection time, then started rising. The average temperature rose 4.4 K from 0 to 8 s. The temporal variation of spanwise-averaged heating rates at $x/L_x = 0.25$ using the semi-infinite method is shown in Fig. 7. The heating rates were calculated for all of the points at this longitudinal position and then averaged. The corresponding results of a two-dimensional laminar computational fluid dynamic (CFD) solution from Ref. 13 are also shown in the figure. Even though the CFD results have their own uncertainty and do not provide the exact results, they will be used to compare the different data-reduction techniques. The semi-infinite heating rates were calculated using both prerun and $t = 0$ s data as the initial temperatures and with and without the correction time given in Eq. (5). For this test the correction time was determined to be 0.89 s. The calculated heating rates using the prerun data resulted in overestimation of the heating rates, by 33–66% compared to CFD, irrespective of whether correction time was used or not. The best results were obtained using no correction time and using data at $t = 0$ s as the initial temperature. These results were within 3–6% of CFD predictions. Use of correction time with data as $t = 0$ s as the initial temperature resulted in overestimation of results at earlier times, whereas the data tended to

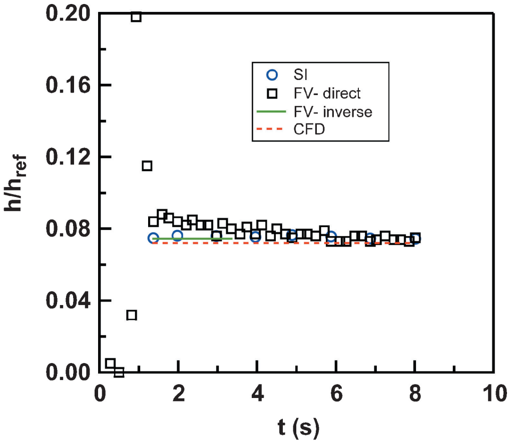

Fig. 8 Temporal variation of spanwise-averaged heating rates at $x/L_x = 0.25$ using finite volume techniques.

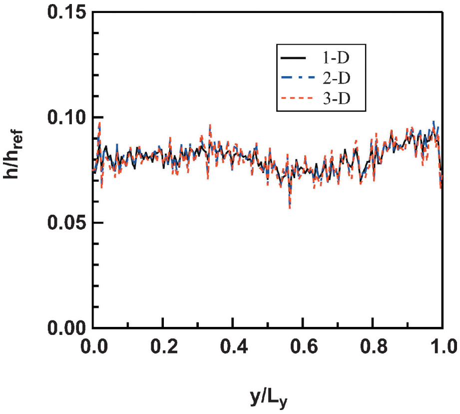

Fig. 9 Comparison of one-, two-, and three-dimensional direct finite volume aeroheating rates at $x/L_x = 0.25$.

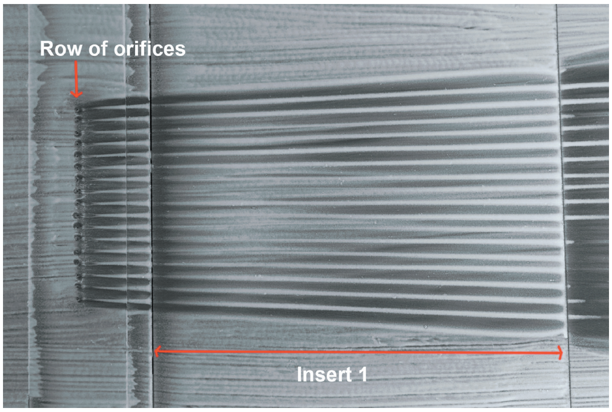

Fig. 10 Oil flow photograph for run with gas injection.

merge with results without correction time at later times (approximately 8 s). The validity of the semi-infinite assumption at this later time is questionable. The semi-infinite assumption for a convective boundary condition is valid for[23]

$$Fo = \alpha t \Big/ L_z^2 \le 0.097 \tag{9}$$

With Macor thermophysical properties at room temperature and a model thickness of 6.35 mm, the semi-infinite assumption is only valid for $t \le 4.9$ s. So, even though reducing data at later times ($t \ge 8$ s) might produce accurate results, but the basic assumption used in the analytical solution is violated. Based on these results, it was concluded that for accurate one-dimensional semi-infinite solutions on slender bodies at low heating rates it is essential to use $t = 0$ s data for the initial condition and not to apply any correction time.

The temporal variation of spanwise-averaged heating rates at $x/L_x = 0.25$ calculated using the direct and inverse one-dimensional finite volume techniques is shown in Fig. 8. CFD results and semi-infinite results without correction time and using $t = 0$ s as initial condition are also shown. The direct finite volume calculations were started at 0 s, and the heating rates were calculated at each instant of time when infrared surface-temperature measurements had been recorded. The heating rates exhibited a sharp increase during the injection process due to rapid temperature rise when the model encountered the flow and then sharply decreased. The calculated heating rates were within ±5.5% of CFD calculations and ±3.5% of semi-infinite results between 5.5- and 8-s time interval. The inverse finite volume results were obtained for the time period between 1.37 and 3.5 s, and the temperature distribution through the model thickness at 1.37 s was appoximated by the solution of Eq. (2) from semi-infinite method assuming no correction time and $t = 0$ s for initial condition. The inverse finite volume results provided a time-invariant solution that was within ±3.5% of CFD solution and 2.1% of semi-infinite results. The use of radiation heat loss term in the energy balance at the model surface Eq. (6e) only made a 0.4% difference in the calculated heat-transfer coefficient for the finite volume techniques. Even though the contribution of radiation loss was almost insignificant for this low heating test, this term should not be excluded for tests at higher heating rates where the model surface temperatures significantly vary from the tunnel walls, and radiation heat transfer becomes significant. The direct finite volume results shown in Fig. 8 exhibited larger temporal noise compared to the inverse finite volume and semi-infinite results. The direct finite volume heating rates are based on both temporal and spatial numerical derivatives of temperature and hence are noisier.

The spanwise variation of convective heat-transfer coefficients at $x/L_x = 0.25$ calculated using one-, two-, and three-dimensional direct finite volume formulations is presented in Fig. 9. The two-dimensional results were calculated at each longitudinal position across the width of the model from $y/L_y = 0$ until $y/L_y = 1$, with the dependence on the x coordinate and the corresponding boundary conditions in this direction eliminated. The heating results presented in the figure were obtained by temporal averaging of data between 2.58 and 3.35 s. The three sets of results coincided with each other and are therefore hard to distinguish from each other in the figure, except at the edges ($y/L_y = 0$ and 1), where the two- and three-dimensional results slightly varied from one-dimensional results because of the imposition of the adiabatic boundary conditions at the edges for the multidimensional formulations. This showed that in a region without significant spatial temperature gradients, such as data at $x/L_x = 0.25$, using one-dimensional analysis was sufficient.

In summary, for regions without significant spatial temperature gradients one-dimensional techniques are sufficient for calculating aeroheating rates, and there was no difference between the various techniques provided that the correct initial temperature conditions were used. It was found that for the semi-infinite technique using the standard prerun image data compared to the data at the beginning of injection of model in to the tunnel could result in significant errors, and that use of correction time was not necessary. Even though the one-dimensional semi-infinite method produced satisfactory results, but it cannot be extended to multidimensional cases and cannot incorporate temperature varying thermophysical properties.

Run with Gas Injection

A run was conducted with gas injection into the boundary layer for tripping the boundary-layer flow. A photograph of the oil flow visualization for a run with similar flow conditions is shown in Fig. 10. The orifices for gas injection and the streamlines corresponding to 18 vortices downstream of the gas injection sites are visible in the photograph. Each gas injection orifice produced two vortices, with the two vortices between adjacent orifices merging together, thus producing 18 vortices for this 17-orifice configuration. A contour plot of the corresponding nondimensionalized convective

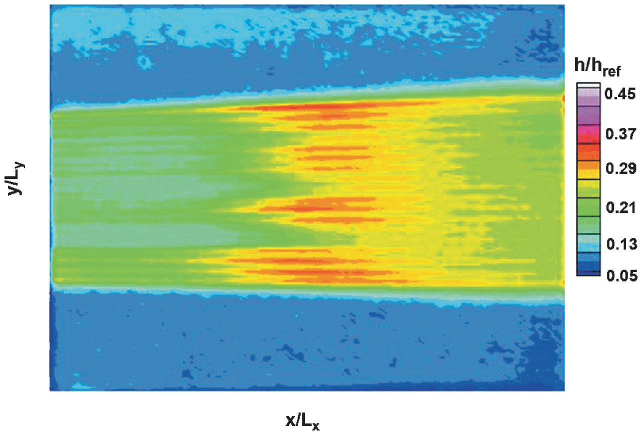

Fig. 11 **Spatial variation of aeroheating rates for run with gas injection using one-dimensional inverse finite volume technique.**

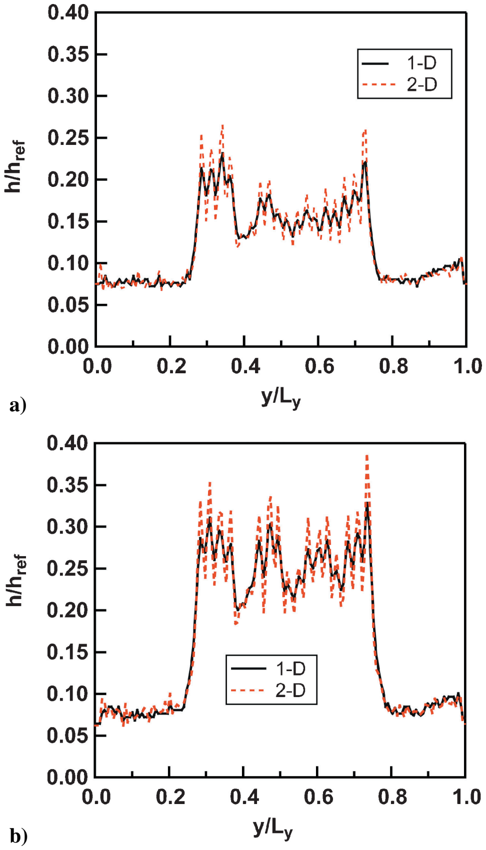

Fig. 13 **Comparison of one- and two-dimensional inverse finite volume aeroheating rates for run with gas injection at x/L_x of a) 0.25 and b) 0.5.**

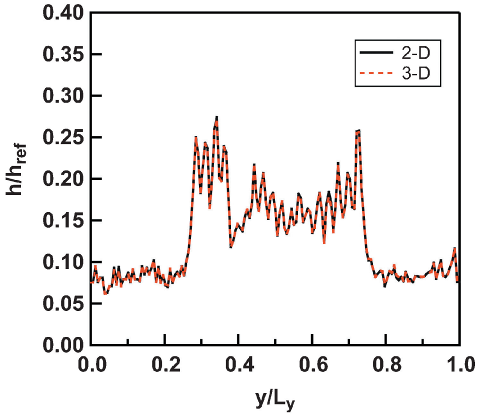

Fig. 12 **Comparison of two- and three-dimensional direct finite volume aeroheating rates at $x/L_x = 0.25$ for run with gas injection.**

heat-transfer coefficients calculated using the one-dimensional inverse finite volume technique is shown in Fig. 11. The traces of 18 streamwise-oriented heating striations downstream of the gas injection sites are visible in the contour plot. Higher heat-transfer rates were generated in the location of the vortices. There is both streamwise and spanwise variation in the heating rates caused by the vortices. The highest heating rates appear between longitudinal locations of $0.25 \leq x/L_x \leq 0.75$. The heating results were consistent with oil flow results in a qualitative sense.

Direct two- and three-dimensional finite volume techniques were compared to determine which formulation would be more appropriate for the given run conditions. The two-dimensional results were calculated at each longitudinal position across the width of the model by eliminating the dependence on the x coordinate and the corresponding boundary conditions in this direction. The comparison of the results at the longitudinal position of $x/L_x = 0.25$ at $t = 3.02$ s is shown in Fig. 12. The heating peaks related to the 18 vortices are visible between y/L_y of 0.2 and 0.8. The heating rates at some vortex locations are as high as 4.8 times the heating rates in the undisturbed regions. Furthermore, it is seen that there is no significant difference between the heating results predicted using either the two- or three-dimensional analysis, with the rms difference between the two sets of results being 1%. Therefore, it was determined that a two-dimensional analysis is sufficient for obtaining heating rates for this run. And because inverse methods yield time-invariant heat-transfer coefficients, two-dimensional inverse finite volume analysis was used for the rest of the study. The comparison of one- and two-dimensional inverse finite volume results for the longitudinal positions of x/L_x of 0.25 and 0.5 are shown in Figs. 13a and 13b, respectively. There is no significant difference between one- and two-dimensional results in the regions without vortices, regions with almost uniform temperatures ($0 \leq y/L_y \leq 0.2$; $0.8 \leq y/L_y \leq 1.0$). There is significant difference between the one- and two-dimensional predicted heating rates in the region with vortices present ($0.2 \leq y/L_y \leq 0.8$). The one-dimensional results underpredict the two-dimensional results at the peak heating locations, the center of vortex locations, and overpredict the two-dimensional results in the cooler region between two adjacent peaks. Lateral heat conduction smears the surface-temperature distribution in regions with sharp heating gradients; heat gets transferred from the higher temperature areas (peaks) at vortex locations to the lower temperature areas between adjacent vortices (valleys), causing reduction of temperature at the peak and increase of temperature at the valleys. When one-dimensional heat transfer is utilized with the measured temperature distributions, the predicted heating rates are lower at the peaks and higher at the valleys. Multidimensional, in this case two-dimensional, heat-transfer analysis can capture gradients better because it accounts for lateral heat conduction. The difference between heating rates calculated using one- and two-dimensional methods along the y axis at longitudinal positions of x/L_x of 0.25 and 0.5 is shown in Figs. 14a and 14b, respectively. There is a nominal ±5% difference between one- and two-dimensional results in the regions with almost uniform temperatures ($0 \leq y/L_y \leq 0.2$; $0.8 \leq y/L_y \leq 1.0$). This is because of inherent noise in the temperature data and how the noise gets amplified differently using the two techniques. But in the region where vortices are present ($0.2 \leq y/L_y \leq 0.8$), there is a distinct and significant difference between one- and two-dimensional results. The one-dimensional method underpredicts and overpredicts the two-dimensional results at the peaks and valley between -15% and $+20\%$, respectively. A contour plot of the corresponding nondimensionalized convective heat-transfer coefficients calculated using the inverse two-dimensional finite volume technique is shown in Fig. 15. Sharper definition of localized heating rates are evident from the two-dimensional results in Fig. 15 compared to the one-dimensional results presented in Fig. 11.

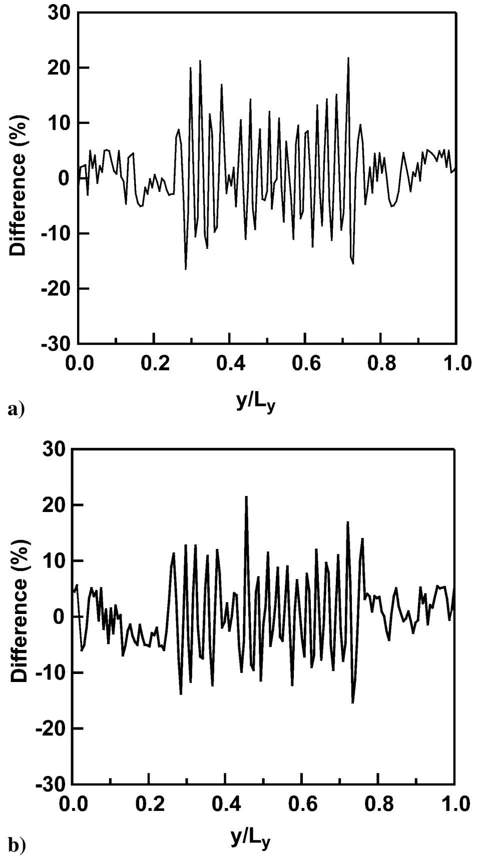

Fig. 14 Relative difference between one- and two-dimensional inverse finite volume aeroheating rates for run with gas injection at x/L_x for a) 0.25 and b) 0.50.

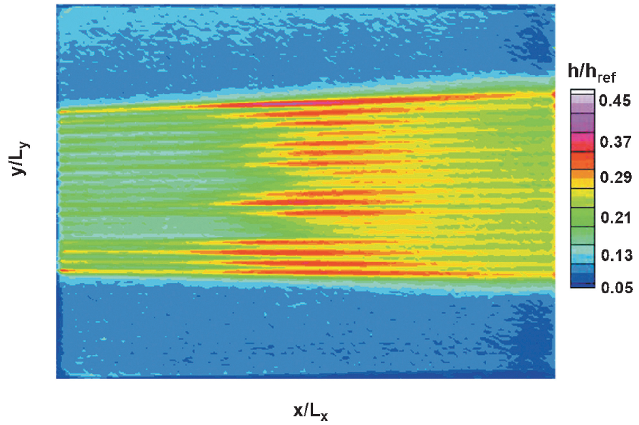

Fig. 15 Spatial variation of aeroheating rates for run with gas injection using two-dimensional inverse finite volume technique.

In summary, it was shown that in regions with significant spatial temperature variations one-dimensional heat-transfer analysis could result in underpredicting and overpredicting heating rates by as much as 20% compared to two-dimensional analysis, and that multidimensional heat-transfer techniques are necessary to predict the heating rates.

Conclusions

Global transient surface temperatures were measured using an infrared thermographic technique on a 0.333-scale model of the Hyper-X forebody in the Langley Research Center 20-Inch Mach 6 Air tunnel. In these tests the effectiveness of vortices generated via gas injection for initiating hypersonic transition on the Hyper-X forebody were investigated. An array of streamwise-orientated heating striations were generated and visualized downstream of the gas injection sites. The striation patterns were attributed to the development of embedded boundary-layer vortices. The use of multidimentional numerical finite volume techniques for calculating aeroheating rates from measured global surface temperatures was investigated. Both direct and inverse finite volume techniques were investigated and compared with the one-dimensional semi-infinite method.

In regions without significant spatial temperature gradients, one-dimensional techniques were sufficient for calculating aeroheating rates, provided that the correct initial temperature conditions were used. It was found that using the standard prerun image data compared to the data at the beginning of injection of model in to the tunnel could result in significant errors. The use of correction time with one-dimensional semi-infinite results did not produce satisfactory results for this low-heating test on a slender body. The semi-infinite results, without correction time and with correct initial temperature conditions, were in close agreement with direct and inverse finite volume results.

In regions with sharp temperature gradients due to the striation patterns two-dimensional finite volume techniques were necessary to more accurately capture heating rates. The use of the one-dimensional technique resulted in heating rate differences of ±20% compared to the two-dimensional technique in the vicinity of vortices because it did not account for lateral heat conduction in the model.

Acknowledgments

This experimental effort was accomplished with the help of many dedicated individuals, a few of whom are mentioned here. Testing was accomplished with the support of G. Gleason, R. Hatten, H. Stotler, K. Hollingsworth, and R. Merski.

References

[1] Miller, C. G., III, "Comparison of Thin-Film Resistance Heat-Transfer Gages with Thin-Skin Transient Calorimeter Gages in Conventional Hypersonic Wind Tunnels," NASA TM-83197, Dec. 1981.

[2] Merski, N. R., "Global Aeroheating Wind-Tunnel Measurements Using Improved Two-Color Phosphor Thermography Method," *Journal of Spacecraft and Rockets*, Vol. 36, No. 2, 1999, pp. 160–170.

[3] Puram, C. K., Daryabeigi, K., and Burkett, C. G., Jr., "Measurement of Steady and Unsteady Temperatures Using Infrared Thermography," *Fundamental Experimental Measurements in Heat Transfer*, ASME HTD-Vol. 179, edited by D. E. Beasley and J. S. Chen, American Society of Mechanical Engineers, New York, 1991, pp. 23–29.

[4] Daryabeigi, K., "Global Surface Temperature/Heat Transfer Measurements Using Infrared Imaging," AIAA Paper 92-3959, July 1992.

[5] De Luca, L., Cardone, G., and Carlomagno, G. M., "Experimental Investigation on Goertler Vortices in Hypersonic Flow," *Computational Methods and Experimental Measurements VI, Vol. 1: Heat and Fluid Flow*, Computational Mechanics Publications, Southampton, England, U.K., 1993, pp. 413–427.

[6] Throckmorton, D. A., Zoby, E. V., Dunavant, J. C., and Myrick, D. L.,"Shuttle Infrared Leeside Temperature Sensing (SILTS) Experiment—STS-28 Preliminary Results," AIAA Paper 90-1741, June 1990.

[7] Blanchard, R. C., Anderson, B. P., Welch, S. S., Glass, C. E., Berry, S. A., Merski, N. R., Banks, D. W., Tietjen, A., and Lovern, M., "Shuttle Orbiter Fuselage Global Temperature Measurements from Infrared Images at Hypersonic Speeds," AIAA Paper 2002-4702, Aug. 2002.

[8] Cook, W. J., and Felderman, E. J., "Reduction of Data from Thin Film Heat Transfer Gages: A Concise Numerical Technique," *AIAA Journal*, Vol. 4, No. 3, 1966, pp. 561, 562.

[9] Hollis, B. R., "User's Manual for the One-Dimensional Hypersonic Aero-Thermodynamic (1DHEAT) Data Reduction Code," NASA CR 4691, Aug. 1995.

[10] Daryabeigi, K., and Huebner, L. D., "Heating Rate Measurements in Hyper-X Wing Gap," NASA TM-2002-211740, July 2002.

[11] Walker, D. G., Scott, E. P., and Nowak, R. J., "Estimation Methods for Two-Dimensional Conduction Effects of Shock-Shock Heat Fluxes," *Journal of Thermophysics and Heat Transfer*, Vol. 14, No. 4, 2000, pp. 533–539.

[12] Coblish, J. J., Smith, M. S., Hand, T., Candler, G. V., and Nompelis, I., "Double-Cone Experiment and Numerical Analysis at AEDC Hypervelocity Wind Tunnel 9," AIAA Paper 2005-0902, Jan. 2005.

[13] Berry, S. A., Auslender, A. H., Dilley, A. D., and Calleja, J. F., "Hypersonic Boundary-Layer Trip Development for Hyper-X," *Journal of Spacecraft and Rockets*, Vol. 38, No. 6, 2001, pp. 853–864.

[14] Micol, J. R., "Langley Aerothermodynamic Facilities Complex: Enhancements and Testing Capabilities," AIAA Paper 98-0147, Jan. 1998.

[15] Modest, M. F., *Radiative Heat Transfer*, McGraw–Hill, New York, 1993, pp. 141, 142.

[16] Hollis, B. R., Horvath, T. J., Berry, S. A., Hamilton, H. H., II, Thompson, R. A., and Alter, S. J., "X-33 Computational Aeroheating Predictions and Comparisons with Experimental Data," *Journal of Spacecraft and Rockets*, Vol. 38, No. 5, 2001, pp. 658–669.

[17] Anderson, D. A., Tannehill, J. C., and Pletcher, R. H., *Computational Fluid Mechanics and Heat Transfer*, Hemisphere, Washington, DC, 1984, Chap. 4.

[18] Özisik, M. N., and Orlande, H. R. B., *Inverse Heat Transfer: Fundamentals and Applications*, Taylor and Francis, New York, 2000, Chap. 2.

[19] Smith, R. H., and Scott, E. P., "2D Non-Uniform, Time Dependent, High Heat Flux Estimates Using Data from Thin Film Sensors and/or PT Measurements," AIAA Paper 2001-0506, Jan. 2001.

[20] Coleman, H. W., and Steele, W. G., Jr., *Experimentation and Uncertainty Analysis for Engineers*, Wiley, New York, 1989.

[21] Hollis, B. R., "Experimental and Computational Aerothermodynamics of a Mars Entry Vehicle," NASA CR-201633, Dec. 1996, pp. 581–582.

[22] Fay, J. A., and Riddell, F. R., "Theory of Stagnation Point Heat-Transfer in Dissociated Air," *Journal of the Aeronautical Sciences*, Vol. 25, No. 2, 1958, pp. 73–85.

[23] Yan, X. T., "On the Penetration Depth in Fourier Heat Conduction," AIAA Paper 2002-2881, June 2002.

T. Lin
Associate Editor

Color reproductions courtesy of NASA Langley Research Center.